Bulletin of the Seismological Society of America, Vol. 103, No. 1, pp. 447–462, February 2013, doi: 10.1785/0120120175

Geometry and Earthquake Potential of the Shoreline Fault, Central California

by Jeanne L. Hardebeck

Abstract The Shoreline fault is a vertical strike-slip fault running along the coastline near San Luis Obispo, California. Much is unknown about the Shoreline fault, including its slip rate and the details of its geometry. Here, I study the geometry of the Shoreline fault at seismogenic depth, as well as the adjacent section of the offshore Hosgri fault, using seismicity relocations and earthquake focal mechanisms. The Optimal Anisotropic Dynamic Clustering (OADC) algorithm (Ouillon *et al.*, 2008) is used to objectively identify the simplest planar fault geometry that fits all of the earthquakes to within their location uncertainty. The OADC results show that the Shoreline fault is a single continuous structure that connects to the Hosgri fault. Discontinuities smaller than about 1 km may be undetected, but would be too small to be barriers to earthquake rupture. The Hosgri fault dips steeply to the east, while the Shoreline fault is essentially vertical, so the Hosgri fault dips towards and under the Shoreline fault as the two faults approach their intersection. The focal mechanisms generally agree with pure right-lateral strike-slip on the OADC planes, but suggest a non-planar Hosgri fault or another structure underlying the northern Shoreline fault. The Shoreline fault most likely transfers strike-slip motion between the Hosgri fault and other faults of the Pacific–North America plate boundary system to the east. A hypothetical earthquake rupturing the entire known length of the Shoreline fault would have a moment magnitude of 6.4–6.8. A hypothetical earthquake rupturing the Shoreline fault and the section of the Hosgri fault north of the Hosgri–Shoreline junction would have a moment magnitude of 7.2–7.5.

Introduction

The Shoreline fault was first recognized by Hardebeck (2010), based on seismicity relocations, as a ~25-km-long, vertical, right-lateral, strike-slip fault running along the coastline near San Luis Obispo, California (Fig. 1). The surface trace of the Shoreline fault was later partially imaged as several scarps in high-resolution bathymetry (Nishenko *et al.*, 2010; Pacific Gas and Electric Company [PG&E], 2011). This fault contributes to the seismic hazard of San Luis Obispo, as well as that of nearby coastal areas that are particularly prone to liquefaction (e.g., Holzer *et al.*, 2005; Lowman, 2009). Additionally, the Shoreline fault runs within 1 km of the Diablo Canyon nuclear power plant. This fault is clearly seismically active, as it has produced approximately 50 recorded $M \leq 3.5$ earthquakes since 1987 (Hardebeck, 2010). In order to include the Shoreline fault in probabilistic seismic hazard assessments (e.g., Working Group on California Earthquake Probabilities [WGCEP], 2008), an estimate of the maximum plausible (or characteristic) earthquake magnitude and an estimate of the fault slip rate are required. The slip rate of the Shoreline fault is currently unknown.

The maximum plausible (or characteristic) earthquake magnitude can be estimated from the largest plausible fault rupture. However, the geometry of the Shoreline fault, and its potential for interaction with other faults, are currently debated. There is no consensus as to whether the Shoreline fault is segmented at seismogenic depths. Hardebeck (2010) proposed an unsegmented fault based on the continuity of seismicity locations at depth. Nishenko *et al.* (2010) proposed three segments based on discontinuities of the surface trace and differences in surface expression. PG&E (2011) interpreted the surface segmentation as extending to seismogenic depths, where they identified small warps in the seismicity locations and differences in the maximum depth of earthquakes.

The southeastern extent of the Shoreline fault is currently unclear, as is the nature of its possible interaction with the San Luis Bay, Oceano, and/or Wilmar Avenue reverse faults (Fig. 1b). These reverse faults are thought to accommodate the uplift of the Irish Hills block near the city of San Luis Obispo (Lettis *et al.*, 1994). The Shoreline fault must

Downloaded from https://pubs.geoscienceworld.org/ssa/bssa/article-pdf/103/1/447/3589131/447.pdf
by University of Memphis, oluwaseun fadugba

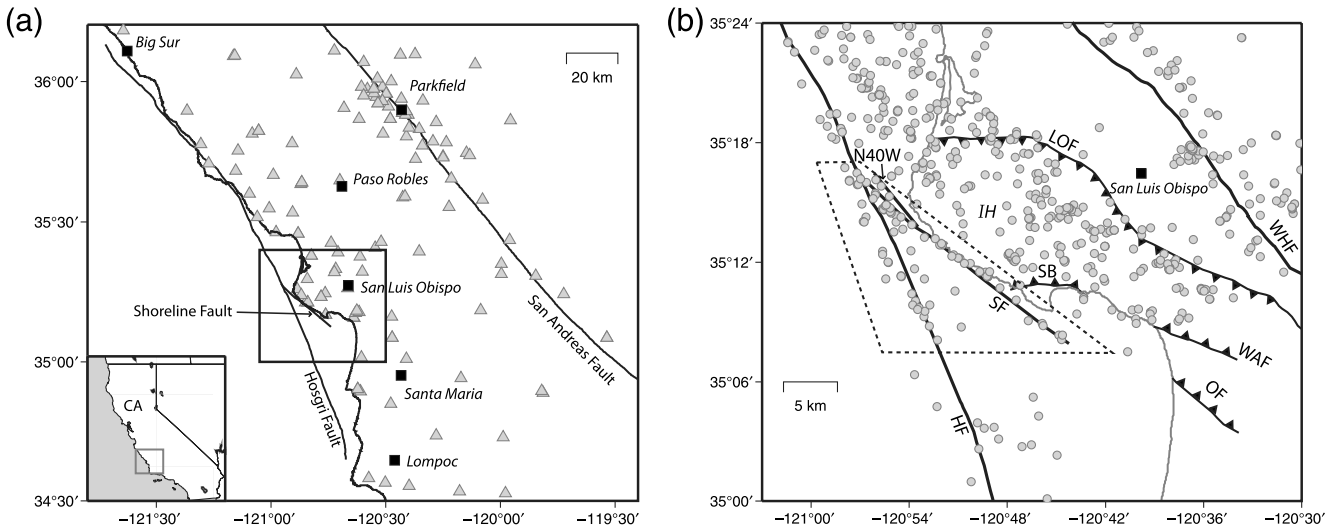

Figure 1 (a) A map of the central California coast, with the location in California (CA) shown in the inset map. Coastline and faults in black; cities, black squares; seismic stations used in this study, gray triangles; box, area in part (b). (b) A map of the earthquakes and faults of the Shoreline fault region. Earthquake locations from Hardebeck (2010), gray circles. Earthquakes within the dashed polygon are relocated in this study. HF: Hosgri fault; IH: Irish Hills; LOF: Los Osos fault; N40W: N40W fault; OF: Oceano fault; SF: Shoreline fault; SB: San Luis Bay fault; WAF: Wilmar Avenue fault; WHF: West Huasna fault. Hosgri and San Andreas faults modified from WGCEP (2008); Shoreline fault from Hardebeck (2010); other faults from (PG&E, 1988, 2011).

extend southeast of its intersection with the San Luis Bay fault, as the largest recorded Shoreline fault earthquake (an M 3.5 on 10 August 2000) occurred southeast of this intersection. A magnetic anomaly observed along the Shoreline fault extends at least another 5 km southeast of the southernmost seismicity (Sliter *et al.*, 2010). The southeastward projection of the Shoreline fault comes onshore near the reverse Oceano fault, which is not the simple continuation of the Shoreline fault due to the change in apparent faulting style.

Additionally, there is not consensus as to whether the northwestern end of the Shoreline fault connects to the Hosgri fault. The ~170-km-long Hosgri fault is the major fault in the region, with a right-lateral slip rate of 1–3 mm/yr (Hanson and Lettis, 1994; Hanson *et al.*, 2004). Hardebeck (2010) interpreted the Shoreline fault as connecting to the Hosgri fault based on the geometry of earthquakes at seismogenic depths, and Watt *et al.* (2011) reached a similar conclusion based on the seismicity and the projection of a magnetic anomaly gradient. Nishenko *et al.* (2010) noted that no northern Shoreline fault surface trace has been observed that would connect the Shoreline to the Hosgri fault, suggesting that there is no active northern Shoreline fault, and the two faults are not connected. Nishenko *et al.* (2010) suggested that the earthquakes that appear to be on the northern Shoreline fault may actually be on an eastward dipping Hosgri fault. Alternatively, these earthquakes may occur on a westward dipping N40W fault, a previously imaged surface feature hypothesized to be a possible northward continuation of the Shoreline fault (PG&E, 2011; Watt *et al.*, 2011).

These differences in the interpreted fault geometry have important implications for the earthquake potential of the Shoreline fault. If the fault is segmented at seismogenic depths, and the segment boundaries pose barriers to earthquake rupture, this would limit the size of the largest possible earthquake to be smaller than the full fault length of ≥25 km would suggest. For example, PG&E (2011) gives the highest weight in their logic tree to a segmented scenario with a maximum rupture length of 16 km. The potential connection with the Hosgri fault also suggests the possibility of an earthquake spanning both faults that would be larger than the Shoreline fault could generate on its own. Although high-frequency energy saturates for large earthquakes, a larger magnitude earthquake produces shaking and damage over a larger area.

I address these unresolved issues regarding the geometry of the Shoreline fault at seismogenic depths, and the Shoreline fault's potential for interaction with the Hosgri fault, using new seismicity relocations and new earthquake focal mechanisms. An objective method is used to determine whether the Shoreline fault seismicity, given the location uncertainty, warrants division into multiple segments or is consistent with a single fault plane. This objective method is used, along with earthquake focal mechanisms, to determine whether or not earthquakes occur on the northernmost Shoreline fault, and hence whether the Shoreline fault is connected to the Hosgri fault.

Methods

I relocate and reinterpret the recorded seismicity to study the geometry of the Shoreline fault and its possible intersection with the Hosgri fault. Earthquake locations can illuminate fault structures at seismogenic depth, but their interpretation is often subjective as fault planes are usually interpreted from the earthquake locations by eye. Alternatively, the Optimal

Downloaded from https://pubs.geoscienceworld.org/ssa/bssa/article-pdf/103/1/447/3589131/447.pdf
by University of Memphis, oluwaseun, fadugba

Anisotropic Dynamic Clustering (OADC) algorithm (Ouillon *et al.*, 2008) can be used to objectively identify the simplest fault geometry that fits all of the earthquake locations to within the location uncertainty. I use the OADC algorithm, along with first-motion focal mechanisms, to determine the fault geometry of the Shoreline fault and the nearby section of the Hosgri fault.

Earthquake Locations and Uncertainty

I relocate ~100 earthquakes occurring along the Shoreline fault and the adjacent section of the Hosgri fault (events inside the dashed polygon in Fig. 1b) between 1 January 1984 and 31 December 2010. Relocations are based on waveform cross-correlation differential times and catalog arrival time picks, using the double-difference programs hypoDD (Waldhauser and Ellsworth, 2000), and tomoDD (Zhang and Thurber, 2003). Cross-correlation was performed on waveforms from stations of the Central Coast Seismic Network (CCSN) and the California Integrated Seismic Network (CISN); catalog arrival times for both networks were obtained from the CISN. All waveforms were inspected by eye for quality, and relative arrival times with correlation coefficients of ≥ 0.8 are used in the relocations. Earthquakes are linked to neighboring events with at least 8 differential times at common stations, with a maximum linking distance of 8 km for catalog differential times and 3 km for cross-correlation differential times. I perform 8 iterations of hypoDD and tomoDD with the catalog picks weighted 10 times the cross-correlation times, to first fit the lower-precision catalog data. Then I perform 8 iterations with the cross-correlation differential times weighted 10 times the catalog times, to refine the relative locations of nearby earthquakes using the higher-precision cross-correlation times. The 3D seismic velocity model of Hardebeck (2010) is used for the tomoDD relocations, and a 1D average of this model is used for the hypoDD relocations. The hypoDD and tomoDD programs return formal errors, but these are likely to underestimate the true uncertainty because they assume that the seismic velocity structure is perfectly known, which is not a good assumption for the study area. Additionally, the formal errors are computed using the final travel-time residuals to approximate the arrival time errors, which may underestimate the uncertainty if the data are overfit.

The earthquake location uncertainty was estimated using synthetic earthquake catalogs instead. Because the "true" locations of synthetic events are known, it is possible to quantify how well the locations are recovered by the relocation procedure, given the distribution of recording stations and random data errors. The error distribution can then be found from multiple realizations of the synthetic data. The synthetic events are constructed to have the same source–receiver geometry as the real earthquakes. The "true" locations of the synthetic events are defined by projecting the catalog earthquake locations onto simplified planar Hosgri and Shoreline faults. Aligning the "true" locations along these planes has no effect on the uncertainty estimates; it merely aids in visualizing the results. Each synthetic event is "recorded" at the same stations as the corresponding real event, travel times are generated using a known "true" velocity model, and realistic travel-time errors are added. Each realization of the synthetic catalog is then relocated using tomoDD following the same procedures as for the real earthquakes, using a velocity model perturbed from the "true" model to reflect velocity model uncertainty. I relocate 300 realizations of the synthetic catalog, each with different random errors in the travel times and velocity model. Any shift in the catalog centroid is removed from the relocated synthetic catalogs, because the goal is to quantify the relative location uncertainty for studying fault geometry. The 95% confidence ellipsoid for each event is determined individually from the distribution of errors of the recovered locations for that event over the 300 realizations. The error is defined as the vector difference between the recovered location and the known "true" location of the synthetic event. The covariance matrix of the 300 errors in the north, east, and vertical directions is used to define the confidence ellipsoid for that event.

The travel-time errors used in the synthetic catalog realizations are based on estimates of the true error in the observed arrival times. The error in the catalog arrival times is estimated by comparing the cross-correlation relative arrival times and the catalog relative arrival times for the same pairs of events, and attributing the differences to errors in the catalog picks (Fig. 2). This assumes that the cross-correlation times are correct, which is a reasonable assumption because the errors in the cross-correlation times are small compared to the errors in the catalog picks. The catalog error is best modeled as an exponential distribution, with the mean equal to 0.3 times the network formal pick error. A consistency check between the cross-correlation relative arrival times, for all sets of three earthquakes linked by cross-correlation times with correlation coefficients of ≥ 0.8, shows that the errors are almost entirely below the sampling rate of 0.01 sec (Fig. 3). Given that the self-consistency check provides a lower bound on the cross-correlation error, and that errors on the order of the sampling rate are likely, an exponential distribution with a mean equal to the sampling rate is used. The velocity model error was estimated from the checkerboard tests of Hardebeck (2010). The percent error for each velocity grid node is chosen from a uniform distribution up to the percent difference between the true and recovered models in the checkerboard tests. Additionally, a systematic velocity model error of up to $\pm 5\%$ is added to the entire model.

OADC

The OADC algorithm (Ouillon *et al.*, 2008) can be used to objectively identify the simplest collection of planar faults that fits all earthquakes in a catalog to within the location uncertainty. Although more complex fault geometries could

Downloaded from https://pubs.geoscienceworld.org/ssa/bssa/article-pdf/103/1/447/3589131/447.pdf
by University of Memphis, oluwaseun_fadugba

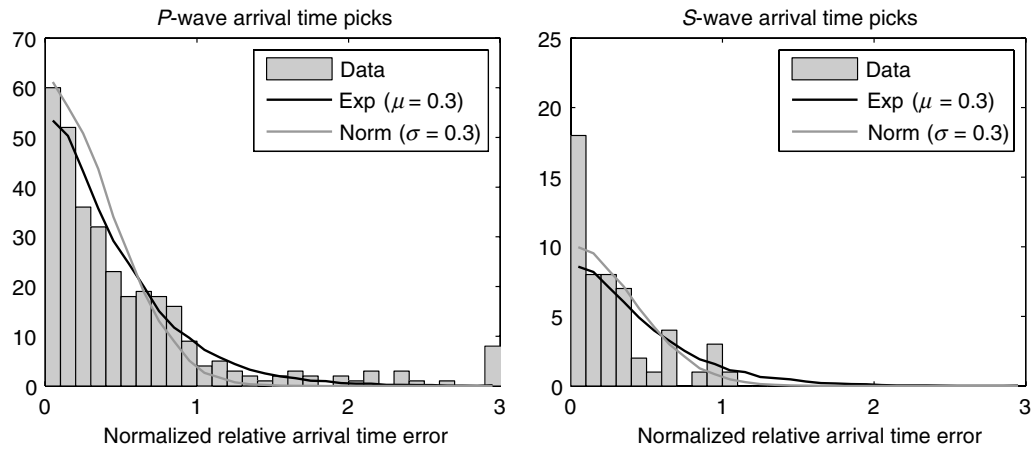

Figure 2. Histograms of the error in relative arrival times for pairs of earthquakes. The error is defined as $|xcor_{i,j} - (tt_i - tt_j)|$ where $xcor_{i,j}$ is the cross-correlation arrival time difference between events i and j, and tt_i and tt_j are the catalog arrival times for those two events, referenced to the same origin times. The assumption is that any error in $xcor_{i,j}$ is so small relative to the errors in tt_i and tt_j that it can be assumed that $xcor_{i,j}$ is correct and that $|xcor_{i,j} - (tt_i - tt_j)|$ reflects the error in $(tt_i - tt_j)$. Picks of different quality are combined in the histograms by normalizing the relative arrival time error by the network formal pick error (quality 0 formal error is 0.1 s; quality 1, 0.2 s; quality 2, 0.5 s; and quality 3, 1.0 s). Shown is the expected distribution of the error in $(tt_i - tt_j)$ if the errors in tt_i and tt_j are each chosen randomly from a normal or exponential distribution, with $\sigma = 0.3$ or $\mu = 0.3$, respectively. The exponential distribution better captures the long-tailed character of the distribution of error in the relative arrival times.

be found that fit the earthquake locations as well or perhaps better, the OADC algorithm follows Occam's razor in favoring the simplest consistent solution. More complex fault geometries, that fit the earthquakes more closely than the location uncertainty, would likely overfit the data, reflecting the random errors in the locations rather than true fault structures. The OADC algorithm partitions the catalog into a given number of sets, such that the distance from the events in each set to the plane representing the set is minimized. The algorithm iteratively updates the best-fitting plane for each set and the assignment of earthquakes to the sets until a stable configuration is reached. The initial planes are chosen randomly and different starting planes may result in different solutions. The number of sets is increased until all events fall on a plane to within the location uncertainty. The only parameter used by the OADC algorithm is the location uncertainty, which is considered tunable by Ouillon *et al.* (2008), but in this work is fixed to the uncertainty estimated from the synthetic catalogs. There are no other parameters that can be tuned.

I implement the OADC algorithm, as described in Ouillon *et al.* (2008), with the following modifications: (1) the algorithm stops when every event is fit to within its 95% confidence ellipsoid, rather than when all events are fit to within

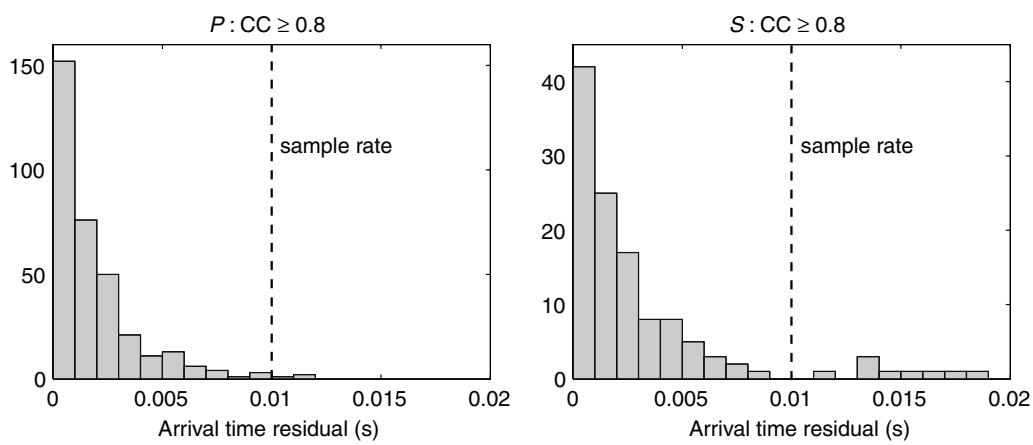

Figure 3. An internal consistency check of the cross-correlation relative arrival times. Histograms show residuals $|xcor_{i,j} + xcor_{j,k} - xcor_{i,k}|$, where $xcor_{i,j}$ is the cross-correlation arrival time difference between events i and j. All sets of three earthquakes linked by cross-correlation times with correlation coefficient of ≥ 0.8 are used. Almost all residuals are less than the sample rate of 0.01 s for both P waves and S waves, with only a few large outliers. The consistency deteriorates for correlation coefficients of < 0.8, indicating that 0.8 is an appropriate threshold for the cross-correlation times. This internal consistency check provides a lower bound on the cross-correlation relative arrival time error.

Downloaded from https://pubs.geoscienceworld.org/ssa/bssa/article-pdf/103/1/447/3589131/447.pdf
by University of Memphis, oluwaseun fadugba

the average location uncertainty. The normal distance from the event to the plane is computed, and compared to the radius of the 95% confidence ellipsoid in the direction normal to the plane. Earthquakes are assigned to the plane that is closest relative to the radius of the ellipse in the normal direction to the plane. Planes with ≤3 events are counted in all processing steps, but are discarded in the final analysis. (2) The algorithm checks if planes are effectively co-planar, and combines any that are. This is to avoid the situation of divided planes, as illustrated in figure 4 of Ouillon *et al.* (2008). Co-planar planes are identified as those whose assigned events are all also consistent with the other plane. (3) The length and width of a plane are defined by the distances between the most distant events assigned to that plane. (4) Repeated runs are performed, with different random starting planes, in order to sample the full solution space. For each run, the initial plane is chosen randomly, and as the number of planes increases, each new plane is chosen randomly. The iterative procedure rapidly corrects these random planes. I consider all unique solutions with the smallest number of planes necessary to fit all of the earthquakes, and compile the statistics of the strike and dip of the planes to quantify the fault plane uncertainty. (5) The OADC algorithm has a tendency to produce spurious subhorizontal planes, as recognized by Ouillon *et al.* (2008), because earthquake locations have less variation in depth than horizontally. I recognize this drawback, but do not attempt to correct it.

Focal Mechanisms

First-motion focal mechanisms are poorly constrained because of the one-sided station coverage of the offshore Shoreline and Hosgri faults (e.g., Hardebeck, 2010). Therefore, I determine composite focal mechanisms, based on the first-motion polarities of all events in three groups: those on the Hosgri fault, those on the southern Shoreline fault (south of 35.23° N), and those on the northern Shoreline fault (north of 35.23° N), with earthquakes assigned to faults according to the OADC results. The northern Shoreline group corresponds to the events that Nishenko *et al.* (2010) hypothesize are actually on the Hosgri fault. Focal mechanisms may allow us to discern which fault these earthquakes are most likely to have occurred on, due to the ~30° difference in fault strike which may be resolvable in the composite mechanisms. First-motion polarities are obtained from the CISN. Take-off angles are found from raytracing in the 3D velocity model of Hardebeck (2010). The focal mechanisms, as well as their uncertainty and quality, are found using the method of Hardebeck and Shearer (2002).

Results

Earthquake Locations and Uncertainty

The relocated earthquake catalogs using hypoDD and tomoDD, while slightly different, both reproduce the basic geometry of the Shoreline fault reported by Hardebeck (2010), a single plane which meets the Hosgri fault at approximately a 30° angle (Fig. 4). The earthquakes along the Hosgri fault appear more diffuse. The average 95% relative location uncertainty is approximately 2 km, both horizontally and vertically. Unsurprisingly, the greatest horizontal location uncertainty is generally in the direction perpendicular to the coastline (Fig. 5). Interestingly, many of the recovered synthetic event locations show systematic offsets from the imposed "true" locations; in particular, the southern Hosgri synthetic events tend to be closer to shore while the northern Hosgri events tend to be further from shore, creating an apparent warp or offset in the recovered locations that is not present in the planar "true" locations. These systematic offsets in the recovered synthetic event locations imply that

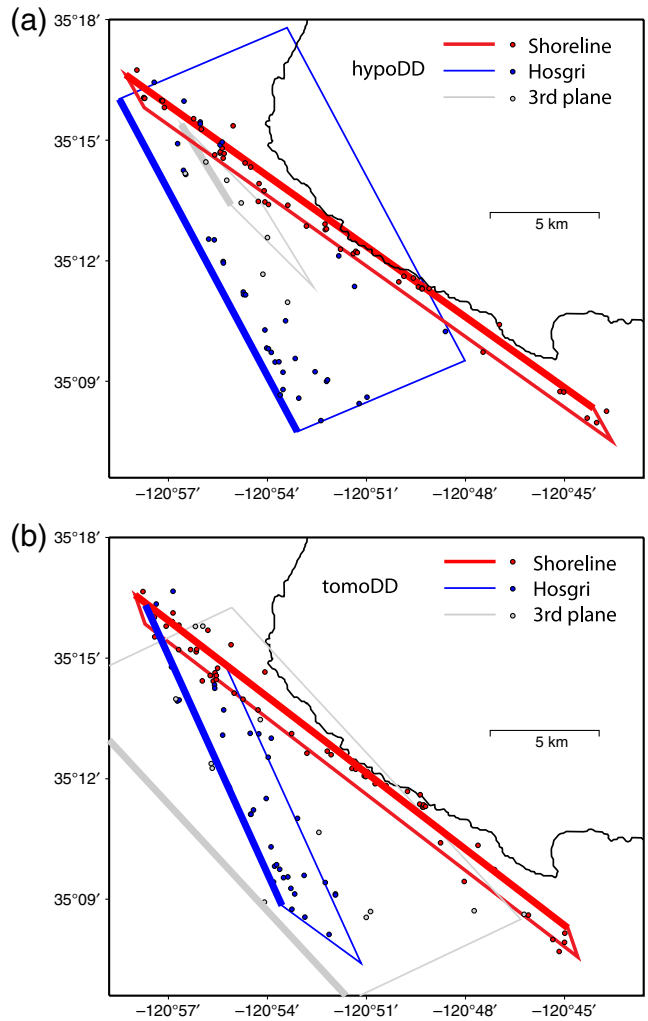

Figure 4. Earthquake relocations and Optimal Anisotropic Dynamic Clustering (OADC) fault plane solutions. The mean fault plane orientation for each of the three planes identified by the OADC algorithm is shown projected into map view, with the top edge indicated by a thicker line. Earthquake locations, circles, with the color matching the color of the plane to which OADC assigns the event. (a) Earthquake locations found using hypoDD. (b) Earthquake locations found using tomoDD. The color version of this figure is available only in the electronic edition.

Downloaded from https://pubs.geoscienceworld.org/ssa/bssa/article-pdf/103/1/447/3589131/447.pdf
by University of Memphis, oluwaseun, fadugba

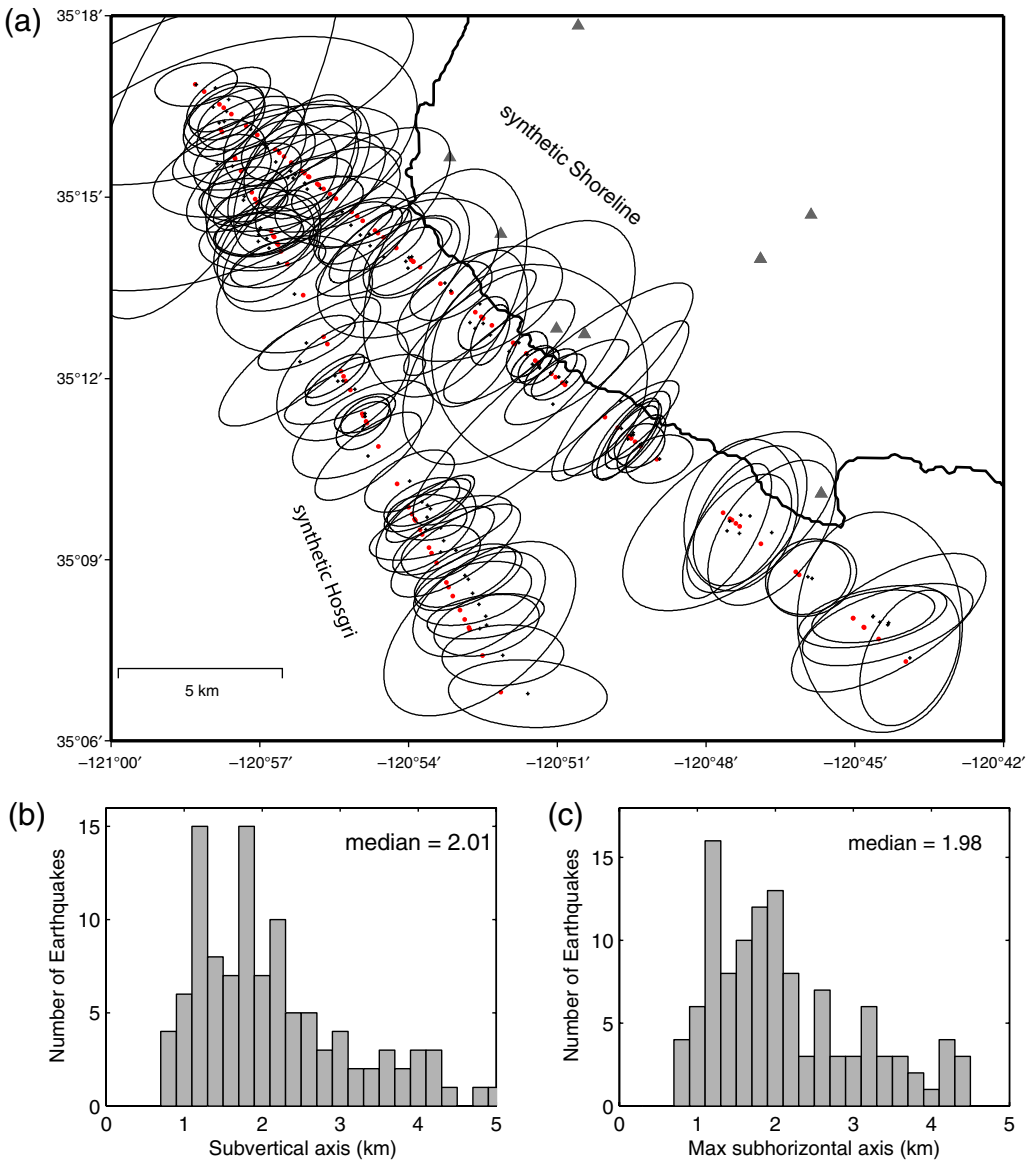

Figure 5. The earthquake location uncertainty, determined from the location errors of synthetic earthquakes. The synthetic earthquakes approximate the real earthquakes, in that each synthetic event is "recorded" at the same stations as the corresponding real event. (a) Dots, the true locations of the synthetic events, defined by projecting the catalog earthquake locations on to simplified planar Hosgri and Shoreline faults; black crosses, the average locations over 300 tomoDD relocation runs with different random arrival time and velocity model errors; 95% confidence ellipsoids (projected into map view) summarize the variability over the suite of runs. Gray triangles; seismic stations. The bottom panels show the distribution of the lengths of the 95% confidence ellipsoid axes, (b) for the most vertical axis (depth uncertainty), and (c) for the largest horizontal axis (horizontal uncertainty). The color version of this figure is available only in the electronic edition.

similar small warps and offsets in the real earthquake locations should not be over-interpreted as they are likely to be artifacts of the poor source-station geometry, and the resulting trade-off between the hypocenter locations and the poorly-constrained velocity model.

OADC

The simplest OADC fault geometry that fits all earthquakes to within their location uncertainty, for either the hypoDD or tomoDD locations, comprises three planes: one clearly corresponding to the Shoreline fault, one corresponding to the Hosgri fault, and a third, unstable, and probably spurious, plane (Figs. 4, 6 and Tables 1, 2). The Shoreline OADC plane is near vertical, and dips very steeply to the southwest. The Hosgri OADC plane dips to the east, towards the Shoreline fault, consistent with the shallow geophysics (e.g., Hanson *et al.*, 2004), although the dip varies greatly between the OADC fits to the hypoDD and tomoDD relocations.

The Shoreline OADC plane orientation is very stable over all solutions, and the northwestern end of the plane extends to the surface trace of the Hosgri fault. The Shoreline

Downloaded from https://pubs.geoscienceworld.org/ssa/bssa/article-pdf/103/1/447/3589131/447.pdf
by University of Memphis, oluwaseun faduyba

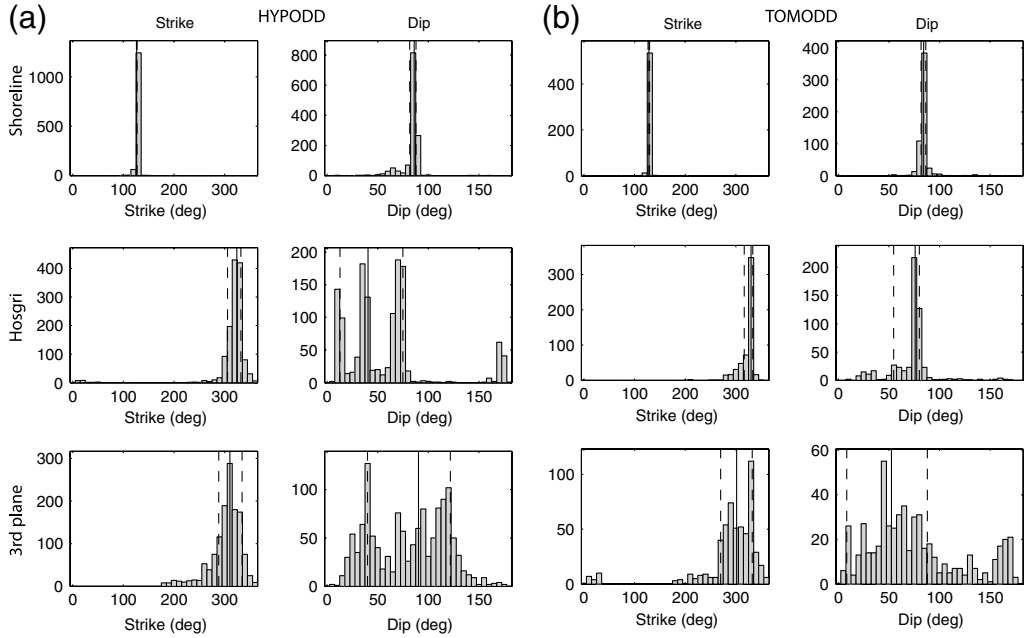

Figure 6. Histograms of the orientations of the three planes identified by the Optimal Anisotropic Dynamic Clustering (OADC) algorithm. The strike and dip of the two planes corresponding in space to the Shoreline and Hosgri faults are shown, along with the strike and dip of the third plane. The fault dips to the right when facing in the strike direction. The circular mean and 1-sigma uncertainty are shown as solid and dashed lines, respectively. The mean plane orientations are shown in Figure 1. (a) For the hypoDD relocated hypocenters, 30,000 runs of the OADC algorithm identified 1317 unique geometries with 3 planes that fit all of the earthquakes to within their location uncertainty. (b) For the tomoDD relocated hypocenters, 30,000 runs of the OADC algorithm identified 552 unique geometries with 3 planes.

OADC plane fits many of the events of the northern Shoreline fault that Nishenko *et al.* (2010) suggest might be on the Hosgri fault and that Watt *et al.* (2011) suggest may be on the N40W fault. The Hosgri OADC plane is less stable, especially in dip, and the northern end does not extend past the intersection with the Shoreline OADC plane. Obviously the Hosgri fault extends north of the intersection, but no seismicity to the north is present in the catalog for the northern continuation to be reflected in the OADC planes. The OADC solutions imply that the Shoreline fault is a single continuous structure that connects to the Hosgri fault.

The third OADC plane is not a robust feature, given that it fits relatively few events compared to the other two planes, and that the plane and the earthquakes assigned to it are different depending on the relocation technique (Fig. 4). The third plane has a location and strike suggesting that it could be a second Hosgri fault strand, which would be consistent with shallow geophysical studies that find two active strands

Table 1
Fault Plane Orientations and Dimensions for the Shoreline and Hosgri Faults*

	Strike (°)	Dip (°)	Rake (°)	Length (km)	Width (km)
Shoreline Fault					
OADC-hypoDD	126 ± 1	86 ± 3		27	11
OADC-tomoDD	128 ± 2	84 ± 2		25	11
FM-South	131 ± 33	86 ± 33	171 ± 33		
FM-North, $d \leq 8$ km	129 ± 32	90 ± 32	178 ± 25		
Hosgri Fault					
OADC-hypoDD	324 ± 13	41 ± 17		17	11
OADC-tomoDD	330 ± 9	76 ± 13		17	9
FM	152 ± 27	73 ± 27	180 ± 24		

*Found from planes fit to the earthquake locations using Optimal Anisotropic Dynamic Clustering (OADC), and from composite focal mechanisms (FM).

Division between northern and southern Shoreline fault at 35.23° N; only events above 8-km depth are used in the focal mechanism for the northern Shoreline fault, because the Hosgri fault or some other structure appears to underlie the northern Shoreline fault (Fig. 9). The strike and dip convention is that the fault dips to the right when facing along the strike direction. The dimensions are given for the mean fault orientation. Uncertainty in OADC plane orientation is the standard deviation from the circular mean.

Downloaded from https://pubs.geoscienceworld.org/ssa/bssa/article-pdf/103/1/447/3589131/447.pdf
by University of Memphis, oluwaseun, fadugba

Table 2
Corners of the Shoreline and Hosgri Fault Optimal Anisotropic Dynamic Clustering (OADC) Planes, for Both the HypoDD and TomoDD Relocated Catalogs

Shoreline OADC plane		Hosgri OADC plane	
HypoDD	TomoDD	HypoDD	TomoDD
−120.9623 35.2635 13.55	−120.9619 35.2641 13.86	−120.8901 35.2966 11.37	−120.9216 35.2478 15.00
−120.9716 35.2771 2.67	−120.9669 35.2761 3.43	−120.9749 35.2670 5.13	−120.9616 35.2719 7.17
−120.7353 35.1388 -1.13	−120.7483 35.1381 0.60	−120.8850 35.1291 3.14	−120.8927 35.1474-0.46
−120.7260 35.1252 9.74	−120.7433 35.1261 11.03	−120.8003 35.1586 9.38	−120.8527 35.1234 7.36

Coordinates are given in: longitude, latitude, and depth in km.

of the fault near the surface (e.g., Hanson *et al.*, 2004). However, rather than the two strands converging at depth into a conventional flower structure, for the hypoDD solutions, the two OADC planes diverge with depth. For the tomoDD solutions, the third plane is subhorizontal, suggesting structures associated with the remnant Farallon subducted slab. However, the third plane consists of earthquakes with an average depth of 5 km, much shallower than the top of the remnant slab, which is at 15–20-km depth in the vicinity of Point Buchon (e.g., Miller *et al.*, 1992). The presence of a subhorizontal plane in the middle of the earthquake depth range is more consistent with the spurious subhorizontal planes recognized by Ouillon *et al.* (2008). Therefore, I consider the third plane to be an artifact, and will not consider it in any further analysis. More than 95% of the earthquakes fall onto either the Shoreline or Hosgri OADC plane in at least one of the two relocated catalogs, indicating that these two planes adequately represent the seismicity to within the location uncertainty and the variability between location methods.

I further validate the Shoreline fault results by demonstrating, using synthetic catalogs, that it is unlikely that multiple fault segments separated by substantial offset could have gone undetected by the OADC algorithm. I generate synthetic "true" earthquake locations by shifting the Shoreline fault earthquakes onto a set of three equal-length vertical planes following the strike of the Shoreline fault but offset horizontally from each other by a variable offset D. The "observed" locations are found by perturbing these "true" locations according to the uncertainty estimates found for the real events. The OADC algorithm is then applied to the "observed" catalog exactly as it was applied to the real earthquakes. The average number of planes found over 3000 OADC realizations is shown as a function of the offset D in Figure 7a. Offsets smaller than ~1 km go largely undetected, but discontinuities smaller than ~1 km are unlikely to be barriers to earthquake rupture (e.g., Harris and Day, 1993, 1999; Wesnousky, 2006, 2008). For $D = 1$ km, at least one offset is detected in >50% of the realization, and this detection ability improves rapidly with increasing D. I also test whether fitting the earthquake locations to within their 95% confidence is appropriate, by repeating the synthetic tests for a range of other confidence levels. Using confidence levels below 95% results in the OADC algorithm typically finding multiple planes when the "true" locations actually lie along a single plane (Fig. 7b). Therefore, attempting to fit the earthquake locations any closer than the 95% confidence level would lead to over-fitting. Any additional planes would be fitting the error in the locations, rather than reflecting the true fault structure.

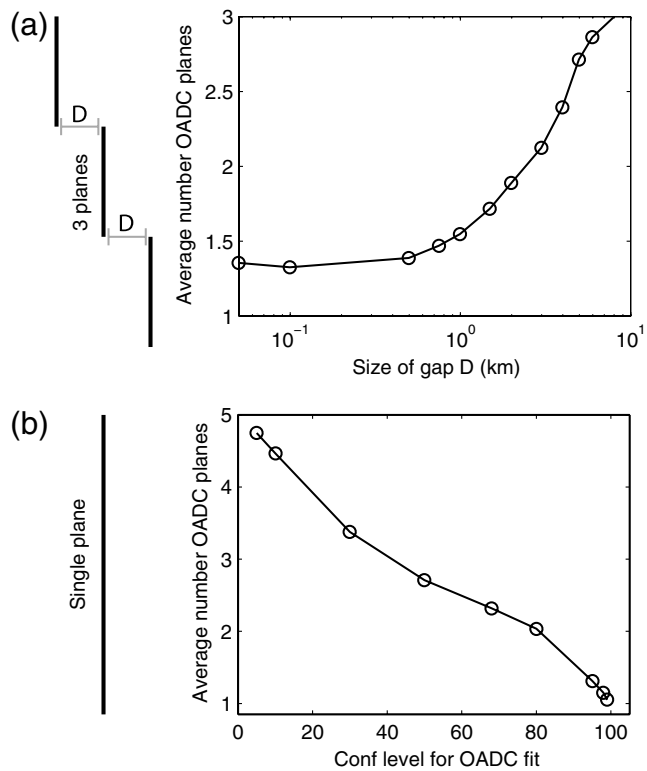

Figure 7. Results from synthetic tests of the Optimal Anisotropic Dynamic Clustering (OADC) algorithm. Synthetic "true" earthquake locations are defined by shifting the Shoreline fault earthquakes onto a series of three vertical planes following the strike of the Shoreline fault but offset horizontally from each other by a variable offset D. The "observed" locations are found by perturbing these "true" locations according to the uncertainty estimates found for the real events. The OADC algorithm is then applied to the "observed" catalog exactly as it was applied to the real earthquakes, for 3000 realizations. (a) Illustration of the fault geometry and the average number of planes found by OADC as a function of the offset D. (b) The average number of planes found by OADC for $D = 0$ (a single plane) when varying the confidence level to which the earthquake locations are fit. More than one plane indicates over-fitting.

Downloaded from https://pubs.geoscienceworld.org/ssa/bssa/article-pdf/103/1/447/3589131/447.pdf
by University of Memphis, oluwaseun, fadugba

Focal Mechanisms

The composite focal mechanism for events along the Hosgri fault is well-constrained, with a quality B solution from the method of Hardebeck and Shearer (2002), and agrees very well with the Hosgri tomoDD OADC plane assuming pure right-lateral strike-slip motion (Fig. 8a). The focal mechanism shows the Hosgri fault dipping to the west, while the Hosgri OADC plane dips to the east, but the first-motion polarities do not constrain the fault plane as well as they constrain the auxiliary plane, and either dip direction would be equally consistent with the polarities. The shallow dip of the Hosgri hypoDD OADC plane is inconsistent with the polarities, so I take the tomoDD OADC plane as the preferred solution. The focal mechanism for the southern Shoreline fault (south of 35.23° N) is not as well-constrained, with a quality D solution, but the mechanism agrees very well with the Shoreline OADC plane, assuming pure right-lateral strike-slip motion (Fig. 8b).

The northern Shoreline composite focal mechanism is made up of the events that both the hypoDD and tomoDD OADC solutions assign to the Shoreline fault, but that Nishenko *et al.* (2010) hypothesize may be on the eastward-dipping Hosgri fault instead. The composite mechanism is marginally well-constrained, with a quality C solution from the method of Hardebeck and Shearer (2002). The composite solution falls in between the OADC planes for the Shoreline and Hosgri faults (Fig. 8c). The Shoreline OADC plane fits the polarities only marginally better, with 6 fewer misfit polarities out of a total of 220 polarities, so this composite mechanism cannot be clearly interpreted as favoring one fault orientation over the other.

Although there are no well-constrained single-event focal mechanisms, the single-event polarities can be used to test whether individual earthquakes are more consistent with the orientation of the Shoreline fault or the Hosgri fault. For each earthquake with ≥8 polarities, I count the fraction of misfit polarities with respect to the Shoreline and Hosgri tomoDD OADC planes, assuming pure right-lateral slip. I quantify the preference for one plane or the other by the difference in the misfit fraction (Fig. 9). For the most part, events along the Hosgri fault agree with the Hosgri OADC plane, and events along the Shoreline fault agree with the

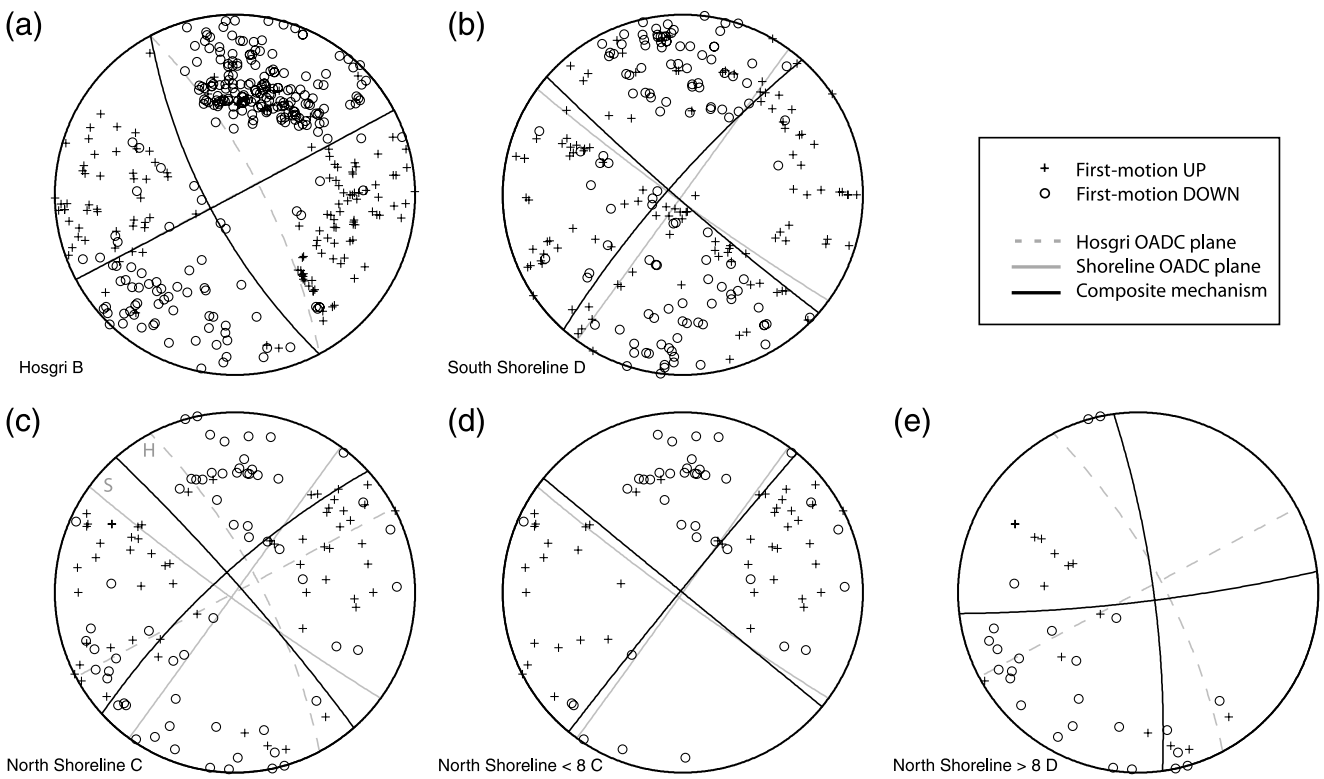

Figure 8. Composite first-motion focal mechanisms. Polarities shown as crosses for upward first arrival; circles for downward first arrival. Black lines: preferred focal mechanism. Gray lines: focal mechanism derived from the OADC plane (tomoDD locations), assuming pure right-lateral rake. (a) All events identified with the Hosgri fault by the OADC procedure, for either the hypoDD or tomoDD locations. The Hosgri OADC solution is shown. (b) All events identified with the southern Shoreline fault (south of 35.23° N) by the OADC procedure, for either the hypoDD or tomoDD locations. The Shoreline OADC solution is shown. (c) All events identified with the northern Shoreline fault (north of 35.23° N) by the OADC procedure, for both the hypoDD and tomoDD locations. The Shoreline OADC solution is shown as solid gray lines; the Hosgri OADC solution is shown as dashed gray lines. (d) Events identified with the northern Shoreline fault by the OADC procedure; only events above 8-km depth. The Shoreline OADC solution is shown. (e) Events identified with the northern Shoreline fault by the OADC procedure; only events deeper than 8-km depth. The Hosgri OADC solution is shown.

Downloaded from https://pubs.geoscienceworld.org/ssa/bssa/article-pdf/103/1/447/3589131/447.pdf
by University of Memphis, oluwaseun, fadugba

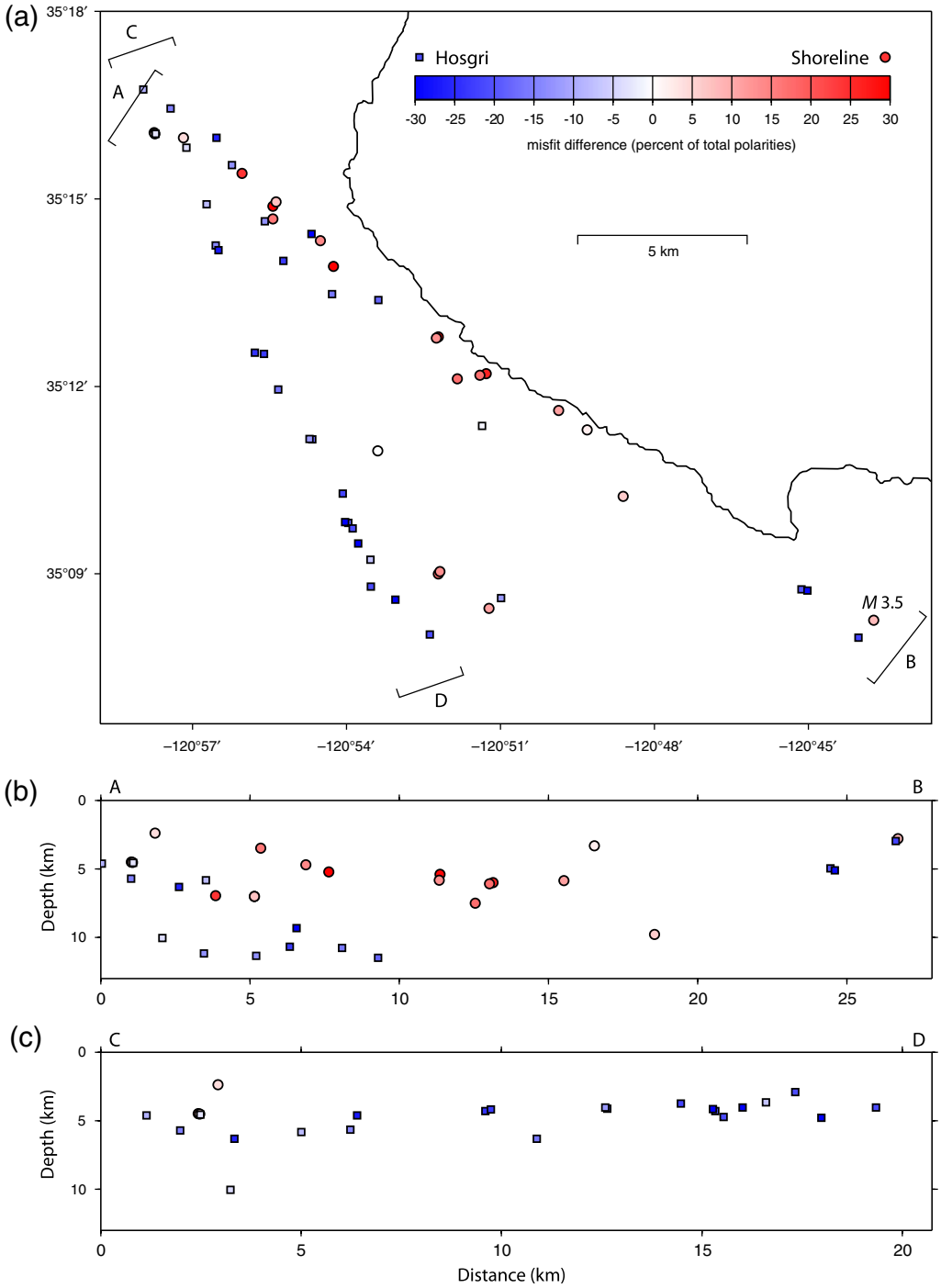

Figure 9. The misfit of single-event first-motion polarities to the focal mechanisms of the Shoreline and Hosgri Optimal Anisotropic Dynamic Clustering (OADC) planes (tomoDD locations), assuming pure right-lateral rake. For each earthquake with at least 8 first-motion polarities, I find the fraction of misfit polarities with respect to the Shoreline and Hosgri OADC planes, and quantify the preference for one plane or the other by the difference in the misfit fraction. Earthquakes shown as circles favor the Shoreline OADC mechanisms, while earthquakes shown as squares favor the Hosgri OADC mechanism. The earthquakes are shown (a) in map view, and in depth sections along the (b) Shoreline, and (c) Hosgri faults. The color version of this figure is available only in the electronic edition.

Shoreline OADC plane, with some exceptions near the southern ends of both planes. The *M* 3.5 earthquake near the southern end of the Shoreline seismicity is better aligned with the Shoreline OADC plane orientation, but some smaller events are not. Most of the shallow to intermediate depth northern Shoreline events are consistent with the Shoreline OADC orientation (Fig. 9). The composite focal mechanism for all northern Shoreline fault earthquakes above 8-km depth also agrees very closely with the orientation of the Shoreline OADC plane (Fig. 8d). However, the deeper events

Downloaded from https://pubs.geoscienceworld.org/ssa/bssa/article-pdf/103/1/447/3589131/447.pdf
by University of Memphis, oluwaseun fadugba

that fall along the northern Shoreline OADC plane are more consistent with the orientation of the Hosgri fault (Fig. 8e).

Fault Geometry

The OADC results imply that the Hosgri fault dips steeply to the east, while the Shoreline fault is essentially vertical. As the two faults approach their intersection, the Hosgri fault would therefore dip towards and under the Shoreline fault (Fig. 10a). The focal mechanisms generally agree with the planar OADC geometry. The shallow-to-intermediate depth northern Shoreline events are consistent with the Shoreline OADC orientation, implying that the vertical planar Shoreline fault extends to the intersection with the Hosgri fault above 8-km depth. The focal mechanisms of deeper earthquakes, however, suggest a slightly more complicated intersection geometry below 8-km depth. The deeper earthquakes that fall along the northern Shoreline OADC plane are more consistent in their focal mechanisms with the orientation of the Hosgri OADC plane, suggesting they are on the Hosgri fault. This would require a non-planar Hosgri fault to underlie more of the northern Shoreline fault than the planar OADC solution would imply (Fig. 10b). The composite focal mechanism for these deep events (Fig. 8e) implies a more north–south strike than the overall strike of the Hosgri fault, consistent with the deep Hosgri fault locally diverging to underlie the Shoreline fault. Alternatively, the deep earthquakes underlying the northern Shoreline fault may represent an additional fault separate from the Hosgri fault (Fig. 10c), or a zone of distributed deformation.

Discussion

The Shoreline fault as defined by seismicity is 25 km long, and its northwestern end extends to the Hosgri fault. There is no gap between the two faults at seismogenic depths, and it appears that the vertical Shoreline fault sits above the east-dipping Hosgri fault near their intersection (Fig. 10). It is unclear why the intersection of the surface traces has not been observed; it may be that the surface trace of the northern Shoreline fault is difficult to image in the marine environment. Alternatively, the surface traces of the faults may not connect, even though the faults are connected at seismogenic depths, as is the case with the intersection of the Hayward and Calaveras faults in the San Francisco Bay area (Manaker *et al.*, 2005). At the Hayward–Calaveras junction, the end of the surface trace of the Hayward fault runs subparallel to the surface trace of the Calaveras fault, while at seismogenic depths the Hayward fault dips towards and merges with the Calaveras. The Shoreline–Hosgri junction would be exactly analogous if the N40W fault trace were the northern end of the Shoreline surface trace, with the seismicity associated with that trace dipping westward to merge with the Hosgri fault.

The geometry of the Shoreline fault, as well as its intersection with the Hosgri fault, appears more simple at seismogenic depths than at the surface, a common feature of strike-slip faults (e.g., Graymer *et al.*, 2007). The surface trace of the southern Shoreline fault appears to have some minor offsets, as well as differences in expression in the bathymetry (Nishenko *et al.*, 2010; PG&E, 2011), so it would be meaningful to refer to three sections of the fault with differences in surface expression. However, there is

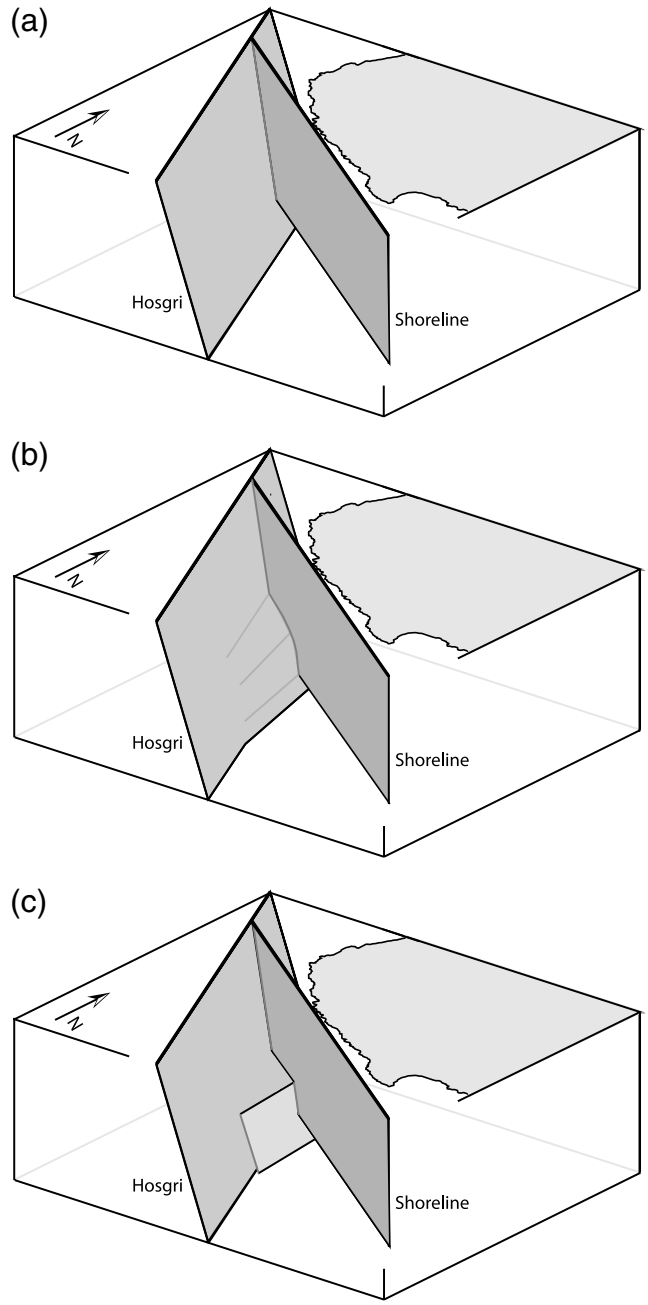

Figure 10. Cartoon of the intersection of the Shoreline and Hosgri faults. Near the intersection, the vertical Shoreline fault lies above the east-dipping Hosgri fault. (a) For the planar Optimal Anisotropic Dynamic Clustering (OADC) geometry. (b) For a similar geometry with a non-planar Hosgri fault underlying the northern Shoreline fault. (c) For a similar geometry with a small north–south trending fault underlying the northern Shoreline fault.

Downloaded from https://pubs.geoscienceworld.org/ssa/bssa/article-pdf/103/1/447/3589131/447.pdf
by University of Memphis, oluwaseun, fadugba

no objective evidence for any discontinuities or segmentation of the Shoreline fault at seismogenic depths, as most earthquakes along its known length fall on a single plane to within their location uncertainty. Discontinuities smaller than ~1 km may be undetected, but would be too small to be barriers to earthquake rupture, as are the < 1 km discontinuities in the surface trace (e.g., Harris and Day, 1993, 1999; Wesnousky, 2006, 2008).

A magnetic anomaly observed along the Shoreline fault implies the presence of serpentinite (Watt *et al.*, 2009; Sliter *et al.*, 2010), which is often associated with weak or creeping faults (e.g., Irwin, 1990). Serpentinites in laboratory experiments at room temperature can exhibit very low coefficients of friction and velocity-strengthening behavior that leads to stable sliding or creep (e.g., Reinen *et al.*, 1994). However, at higher temperatures and pressures representative of seismogenic depths, the strength of serpentinite increases to nearly that of characteristically strong rocks (Moore *et al.*, 1997). Serpentinites can exhibit velocity-weakening behavior at higher slip velocities (Reinen *et al.*, 1994), implying that earthquakes nucleating elsewhere on the fault could continue propagating through the serpentinite. The non-zero fault strength ensures that there would be shear stress on the serpentinite patches to drive continued rupture, even if they were usually creeping. Serpentinites also tend towards velocity-weakening behavior at higher temperatures (Moore *et al.*, 1997), implying that earthquakes could potentially nucleate in serpentinite at depth. Nucleation clearly can occur on the Shoreline fault, given the observed seismicity on the fault, including an M 3.5 earthquake. Therefore, the Shoreline fault should be considered capable of nucleating and propagating large earthquakes.

The size of the Shoreline fault plane determined by the OADC algorithm can be used to estimate the magnitude of a hypothetical earthquake rupturing the entire fault (Table 3). The OADC plane is 25 km long with a width of 11 km, and comes within at least 0.5 km of the surface (Table 2), consistent with the expression of most of the fault on the seafloor. Assuming a 3 MPa stress drop, the moment magnitude would be 6.7. Scaling relationships with either rupture length or rupture area for a strike-slip fault (Wells and Coppersmith, 1994) give moment magnitudes of 6.4–6.5. Extending the southern end of the Shoreline fault to the coast adds 10 km to the southeastern end of the fault, increasing the moment magnitude to 6.8 for the constant stress drop approach, and to 6.6 for both scaling approaches. Given the connection between the Shoreline and Hosgri faults at seismogenic depths, it should be possible for a hypothetical earthquake nucleating on the Shoreline fault to continue rupturing to the north onto the Hosgri fault. Examples of earthquakes starting on a smaller fault and continuing onto a nearby larger fault include the 2002 M 7.9 Denali earthquake (e.g., Eberhart-Phillips *et al.*, 2003) and the 2001 M 7.8 Kokoxili (or Kunlun) earthquake (e.g., Klinger *et al.*, 2005). This scenario could extend the rupture length an additional ~100 km to the WGCEP (2008) northern termination of the Hosgri fault near Big Sur. This hypothetical earthquake would have a moment magnitude of 7.2–7.5 (Table 3), compared to a magnitude 7.3–7.7 if the entire WGCEP (2008) Hosgri fault were to rupture.

Given that rupture directivity can greatly influence the spatial distribution of ground shaking (e.g., Aagaard *et al.*, 2010), it is important to consider also whether a southward-propagating earthquake on the Hosgri fault could branch onto the Shoreline fault. Kame *et al.* (2003) present a generic model of dynamic rupture on a main fault with a splay fault. They find that whether or not a rupture branches onto the splay fault depends on the stress orientation. Unfortunately, the stress orientation at the Shoreline–Hosgri intersection is unknown. The single event focal mechanisms do not have the quality or quantity necessary for a stress inversion. The composite mechanisms constrain only the quadrants of the principal stresses (McKenzie, 1969), and so the maximum compressive stress could be oriented anywhere from 0° to 60° to the Hosgri fault strike, in the sense to drive right-lateral slip. McLaren and Savage (2001) find that the average orientation of focal mechanism P axes over a larger region is ~43° to the strike of the Hosgri fault, but do not invert for

Table 3
Fault Dimensions for Four Different Hypothetical Earthquakes

	L (km)	W (km)	M_w ($\Delta\sigma = 3$ MPa)	M_w (W&C length)	M_w (W&C area)
Shoreline, seismicity	25	11	6.7	6.4	6.5
Shoreline, to coast	35	11	6.8	6.6	6.6
Shoreline + Hosgri	130	11	7.2	7.5	7.2
Hosgri, WGCEP segment	170	11	7.3	7.7	7.3

Four scenario earthquakes: a rupture of the Shoreline fault as defined by the seismicity; a rupture of the Shoreline fault continued southeast to the coastline; a rupture of the Shoreline fault along with the section of the Hosgri fault from the Shoreline–Hosgri junction to the northern WGCEP (2008) fault endpoint near Big Sur; and a rupture of the whole WGCEP (2008) Hosgri fault length. The fault width is taken from the Optimal Anisotropic Dynamic Clustering OADC fit to the Shoreline fault. The moment magnitude is determined either from assuming a 3 MPa stress drop and the appropriate stress drop equations for a strike-slip fault (e.g., Lay and Wallace, 1995), or using the moment-length and moment-area regressions from Wells and Coppersmith (1994).

Downloaded from https://pubs.geoscienceworld.org/ssa/bssa/article-pdf/103/1/447/3589131/447.pdf
by University of Memphis, oluwaseun, fadugba

stress orientation. The World Stress Map (Heidbach *et al.*, 2008) includes only two borehole breakouts nearby: one near San Luis Obispo with a maximum compressive stress axis oriented 53° to the strike of the Hosgri fault, and one west of the Hosgri fault with maximum compressive stress oriented 81° to the Hosgri strike, which is obviously not representative of the Hosgri–Shoreline junction because it predicts left-lateral motion on the Shoreline fault.

The Kame *et al.* (2003) model shows that a compressive branch oriented ~30° from the main fault, such as the Shoreline fault branching off of the Hosgri fault, is favored in the prestress field if the maximum compressive stress is at an angle < 45° to the strike of the main fault, which is plausible. Dynamic rupture in this case branches onto the splay fault, but the rupture on the splay fault is arrested by the stress shadow from continued rupture on the main fault under most conditions. This suggests that southward directed rupture on the Hosgri fault would probably not successfully branch onto the Shoreline fault.

However, there are several simplifications in the Kame *et al.* (2003) model that may make the results inapplicable to the specific case of the Hosgri and Shoreline faults. First, the model is 2D, meaning that any effects from 3D structure are not modeled. The Hosgri–Shoreline intersection has a complicated 3D structure, with the splay fault sitting above the dipping main fault, and a possible non-planar Hosgri fault, or another structure, at depth (Fig. 10). Second, the fault strength in the Kame *et al.* (2003) model follows a simple slip-weakening law, and the main and splay faults are assumed to have the same strength. The Hosgri and Shoreline faults could have very different constitutive properties, as there appears to be serpentinite along the Shoreline fault. The assumed slip-weakening strength evolution in the Kame *et al.* (2003) model is quite different from the laboratory constitutive properties of serpentinite, which exhibits depth-dependent strength, and velocity- and temperature-dependent transitions from velocity strengthening to velocity weakening behavior (Reinen *et al.*, 1994; Moore*et al.*, 1997). Third, the timing and effects of prior earthquakes on each fault are not considered. Modeling by Duan and Oglesby (2007) shows that prior earthquakes have a significant effect on the stress around the branch point. Schwartz *et al.* (2012) conclude that the relatively longer time since the most recent event was the primary factor that caused the 2002 M 7.9 Denali, Alaska, earthquake to branch onto the Totschunda fault rather than continuing on the main Denali fault.

When considering the interaction between the Shoreline fault and other faults, it is important to remember that the primary mode of deformation in the San Luis Obispo area is strike-slip faulting. The Hosgri fault slip rate of 1–3 mm/yr (Hanson and Lettis, 1994; Hanson *et al.*, 2004) is an order of magnitude greater than the 0.1–0.2 mm/yr uplift rate of the Irish Hills (Hanson *et al.*, 1994). Given that the Shoreline fault is connected to the Hosgri fault, it most likely functions as part of the dominant strike-slip system. The slip rate and cumulative offset of the Hosgri fault are thought to diminish to the south, reaching zero offshore of Lompoc (Hanson *et al.*, 2004; Jachens *et al.*, 2009), and so its slip must be transferred eastward to other faults of the plate boundary system. The Shoreline fault most likely transfers some of this strike-slip motion southeastward. The current configuration of the Shoreline and Hosgri faults is inherently unstable for large amounts of slip, despite the apparent lithological contrast across the Shoreline fault (Nishenko *et al.*, 2010) that suggest non-negligable vertical or horizontal offset. The fault junction could be maintained through dip-slip faulting, deflection of the fault planes, and/or distributed deformation. Alternatively, the Shoreline fault could be a reactivated preexisting fault.

The Shoreline fault may interact with the system of reverse faults bounding the Irish Hills (Lettis *et al.*, 1994). The Shoreline fault possibly crosses and perhaps truncates the reverse San Luis Bay fault, and runs subparallel to the reverse Los Osos, Wilmar Avenue, and Oceano faults (Fig. 1). The geometry of the Shoreline fault with respect to these faults is not consistent with that of a tear fault, which would strike perpendicular to and connect offset reverse faults. The Shoreline and Hosgri faults may instead accommodate some of the uplift of the Irish Hills block relative to the offshore Santa Maria Basin. Because the uplift rate is an order of magnitude smaller than the strike-slip rate of the Hosgri fault, the motion of the Hosgri fault would still be strike-slip with only minor obliquity. The Shoreline fault is a logical candidate for a bounding fault for the Irish Hills, given the steep topography along the very straight coastline. It is such a logical candidate based on the geomorphology, that prior to the discovery of the Shoreline fault by Hardebeck (2010) a reverse fault was hypothesized in its exact location (Nitchman and Slemmons, 1994). If the Shoreline fault has accommodated some vertical motion, its current strike-slip rate must be greater, given that the focal mechanisms are strike-slip.

Some bounds can be placed on the current ratio of the vertical to horizontal slip rate of the Shoreline fault. The greatest amount of reverse slip encompassed by the confidence bounds of the southern Shoreline fault composite focal mechanism is a rake of 138° (Table 1). This rake bounds the ratio of vertical to horizontal slip to be $v/h \leq 0.9$. An upper bound can be put on the vertical slip rate, $v \leq 0.2$ mm/yr, the uplift rate of the Irish Hills. Unfortunately, these bounds cannot place any meaningful constraints on the horizontal slip rate, h, without a non-zero lower bound on either v/h or v.

The approximately 50 $M \leq 3.5$ recorded earthquakes on the Shoreline fault are inadequate to extrapolate to the rate of larger events, especially without knowing whether or not there are characteristic large earthquakes that occur more frequently than extrapolation of smaller events may suggest (e.g., Schwartz and Coppersmith, 1984; Parsons and Geist, 2009). However, this extrapolation may provide an approximate lower bound, without having to resolve the existence or non-existence of characteristic earthquakes. In the characteristic earthquake model (e.g., Schwartz and Coppersmith, 1984), the extrapolation of the rate of smaller events would

Downloaded from https://pubs.geoscienceworld.org/ssa/bssa/article-pdf/103/1/447/3589131/447.pdf
by University of Memphis, oluwaseun, fadugba

by definition underestimate the rate of larger events. In the alternative model, earthquake occurrence follows the Gutenberg–Richter law over all magnitudes, but temporal earthquake clustering leads to different earthquake rates over different time scales (Page *et al.*, 2008). In such a model, a short earthquake catalog would usually underestimate the total earthquake rate, as it is unlikely to capture a period of intense earthquake clustering (Page *et al.*, 2008). The recorded earthquakes on the Shoreline fault do not exhibit strong temporal clustering, so it is reasonable to assume that an extrapolation of the current rate would provide a lower bound on the long-term earthquake rate.

A rough lower bound is placed on the rate of $\mathbf{M} \geq 6.7$ earthquakes on the Shoreline fault by extrapolating from the events that the OADC algorithm identified with the Shoreline fault. The EMR method (Woessner and Wiemer, 2005) is used to identify the magnitude of completeness of 1.6, the Gutenberg–Richter *a*-value and *b*-value are fit using maximum likelihood, and the Gutenberg–Richter distribution is extrapolated to larger magnitudes (Fig. 11). From this extrapolation, the rate of $\mathbf{M} \geq 6.7$ earthquakes is constrained to be $\geq 1.5 \times 10^{-5}$ events/yr, which corresponds approximately to a slip rate bound of ≥ 0.04 mm/yr, assuming most of the slip is accommodated in $\mathbf{M}$ 6.7 earthquakes. An upper bound can be found from the assumption that the Shoreline fault, functioning as part of the Hosgri fault system, would not slip faster than the Hosgri fault north of the junction. This places a bound on slip rate of ≤ 3 mm/yr, corresponding to $\leq 1.0 \times 10^{-3}$ events/yr assuming $\mathbf{M}$ 6.7 earthquakes. The possible slip rate ranges across two orders of magnitude, which is too uncertain for meaningful hazard estimates. Slip rate is therefore a key parameter that must be more tightly constrained in order to include the Shoreline fault in probabilistic seismic hazard assessment.

Conclusions

The geometries of the Shoreline fault at seismogenic depth, and of the adjacent section of the Hosgri fault, are constrained from seismicity relocations and composite first-motion focal mechanisms. The OADC method, which objectively determines planar fault geometry from the seismicity locations, identifies the Shoreline fault as a single continuous structure that connects to the Hosgri fault. The Hosgri fault dips steeply to the east, while the Shoreline fault is essentially vertical, so the Hosgri fault dips towards and under the Shoreline fault as the two faults approach their intersection. The focal mechanisms generally agree with pure right-lateral strike-slip on the OADC planes, but suggest either a non-planar deep Hosgri fault or some other structure underlying the northern Shoreline fault (Fig. 10b).

These results support the interpretation of Hardebeck (2010) that the Shoreline fault is a continuous planar fault at seismogenic depth, rather than the interpretation of Nishenko *et al.* (2010) and PG&E (2011) that the fault is divided into three segments by boundaries that would act as barriers to earthquake rupture. The results also support the interpretation of Hardebeck (2010) that the northern Shoreline fault connects to the Hosgri fault. The hypothesis of Nishenko *et al.* (2010) that the earthquakes that appear to be on the northern Shoreline fault are actually on an east-dipping Hosgri fault may be partially correct, as the deep events underlying the northern Shoreline fault could be on the Hosgri fault. However, the earthquakes above ~8-km depth delineate the northern Shoreline fault extending to the Hosgri fault. The Shoreline fault most likely accommodates the transfer of strike-slip motion between the Hosgri fault and other faults of the plate boundary system to the east.

The geometry of the Shoreline fault can be used to estimate its earthquake potential, although the probability

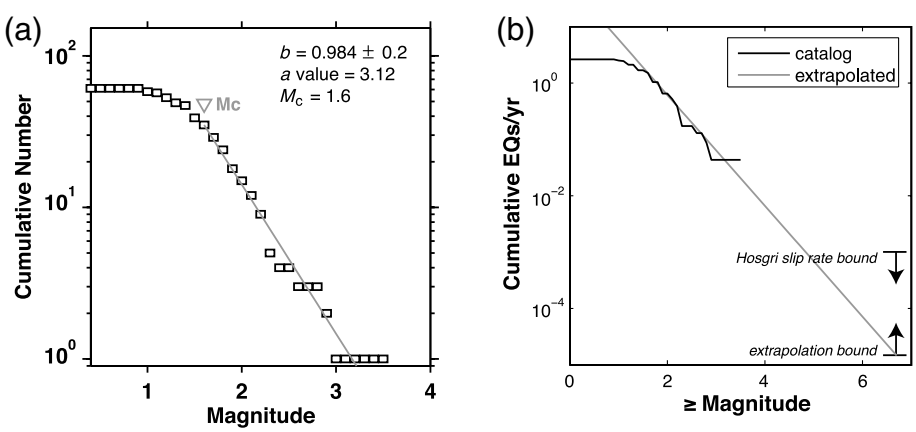

Figure 11. Magnitude frequency distribution for earthquakes on the Shoreline fault. (a) Cumulative distribution of magnitudes for earthquakes identified by the Optimal Anisotropic Dynamic Clustering (OADC) algorithm as being on the Shoreline fault. Magnitude of completeness, M_c, and Gutenberg–Richter distribution parameters, *a* and *b*, found using the ZMAP software (Wiemer, 2001) and the EMR method of Woessner and Wiemer (2005). (b) Number of events per year, black line from the catalog and gray line from extrapolation using the Gutenberg–Richter parameters. The extrapolation to $\mathbf{M}$ 6.7 provides a lower bound on the rate of $\mathbf{M} \geq 6.7$ earthquakes. An upper bound is estimated by assuming that the Shoreline fault does not slip faster than the Hosgri fault.

Downloaded from https://pubs.geoscienceworld.org/ssa/bssa/article-pdf/103/1/447/3589131/447.pdf
by University of Memphis, oluwaseun fadugba

of a large earthquake cannot be reliably estimated because the slip rate is unknown. A hypothetical earthquake rupturing the entire known length of the Shoreline fault could have a moment magnitude of 6.4–6.8. Because the Shoreline and Hosgri faults are connected at seismogenic depths, a rupture nucleating on the Shoreline fault could continue propagating onto the Hosgi fault. A hypothetical earthquake rupturing the Shoreline fault and the section of the Hosgri fault north of its junction with the Shoreline fault could have a moment magnitude of 7.2–7.5. Generic 2D modeling of dynamic rupture on fault branches suggests that a rupture on the Hosgri fault should not branch onto the Shoreline fault, but this type of modeling does not capture the 3D geometry of the Shoreline–Hosgri intersection, the complex constitutive properties implied by the apparent presence of serpentinite in the Shoreline fault zone, or the unknown earthquake history of both faults.

Data and Resources

The merged CISN/CCSN phase catalog 1984–2010 was obtained from the Northern California Earthquake Data Center (NCEDC; http://www.ncedc.org/ncedc/catalog-search.html, last accessed January 2011). The CISN/NCSN waveforms are also obtained from the NCEDC, and CISN/SCSN waveforms are obtained from the Southern California Earthquake Data Center (http://www.data.scec.org/research-tools/index.html, last accessed January 2011). Waveforms from the CCSN stations were obtained through the NCEDC for events after 5 September 2006. Waveforms from CCSN stations for events prior to 5 September 2006 were obtained from PG&E. The WGCEP UCERF3 report can be found online at http://pubs.usgs.gov/of/2007/1437/ (last accessed May 2012). The Sliter *et al.* USGS Open File Report can be found online at http://pubs.usgs.gov/of/2009/1100/ (last accessed May 2012). Lowman's thesis was downloaded from http://digitalcommons.calpoly.edu/erscsp/2 (last accessed May 2012). PG&E's report on the Shoreline Fault was downloaded from http://www.pge.com/myhome/edusafety/systemworks/dcpp/shorelinereport (last accessed May 2012).

Acknowledgments

I thank Janet Watt, Bob Simpson, Andy Michael, and two anonymous reviewers for helpful comments on an earlier version of this manuscript. I am grateful to Stephan Husen for helpful suggestions on how to estimate earthquake location uncertainty from synthetic data, and for ideas about modifications to the OADC algorithm. I thank the staffs of the CISN and the CCSN for collecting and providing the earthquake waveforms and phase data, and Haijiang Zhang and Felix Waldhauser for making their earthquake relocation codes available. This research was funded in part by the USGS/PG&E Cooperative Research and Development Agreement.

References

Aagaard, B. T., R. W. Graves, A. Rodgers, T. M. Brocher, R. W. Simpson, D. Dreger, N. A. Petersson, S. C. Larsen, S. Ma, and R. C. Jachens (2010). Ground-motion modeling of Hayward Fault scenario earthquakes; Part II, Simulation of long-period and broadband ground motions, *Bull. Seismol. Soc. Am.* **100,** 2,945–2,977.

Duan, B., and D. D. Oglesby (2007). Nonuniform prestress from prior earthquakes and the effect on dynamics of branched fault systems, *J. Geophys. Res.* **112,** 18 pp., B05308, doi: 10.1029/2006JB004443.

Eberhart-Phillips, D., P. J. Haeussler, J. T. Freymueller, A. D. Frankel, C. M. Rubin, P. Craw, N. A. Ratchkovski, G. Anderson, G. A. Carver, A. J. Crone, T. E. Dawson, H. Fletcher, R. Hansen, E. L. Harp, R. A. Harris, D. P. Hill, S. Hreinsdóttir, R. W. Jibson, L. M. Jones, R. Kayen, D. K. Keefer, C. F. Larsen, S. C. Moran, S. R. Personius, G. Plafker, B. Sherrod, K. Sieh, N. Sitar, and W. K. Wallace (2003). The 2002 Denali fault earthquake, Alaska: A large magnitude, slip-partitioned event, *Science* **300,** 1,113–1,118.

Graymer, R. W., V. E. Langenheim, R. W. Simpson, R. C. Jachens, and D. A. Ponce (2007). Relatively simple through-going fault planes at large-earthquake depth may be concealed by the surface complexity of strike-slip faults, *Geol. Soc. London Special Publications* **290,** 189–201.

Hanson, K. L., and W. R. Lettis (1994). Estimated Pleistocene slip rate for the San Simeon Fault Zone, south-central coastal California, in *Seismotectonics of the Central California Coast Ranges*, Geol. Soc. Am. Special Paper, I. B. Alterman, R. B. McMullen, L. S. Cluff, and D. B. Slemmons (Editors), Vol. **292**, 133–150.

Hanson, K. L., W. R. Lettis, M. K. McLaren, W. U. Savage, and N. T. Hall (2004). Style and rate of Quaternary deformation of the Hosgri fault zone, offshore south-central California, in *Evolution of Sedimentary Basins/Offshore Oil and Gas Investigations—Santa Maria Province*, M. A. Keller (Editor), *U.S. Geol. Surv. Bull. 1995-BB*, 33 pp.

Hanson, K. L., J. R. Wesling, W. R. Lettis, K. I. Kelson, and L. Mezger (1994). Correlation, ages, and uplift rates of Quaternary marine terraces: South-central coastal California, in *Seismotectonics of the Central California Coast Ranges*, Geol. Soc. Am. Special Paper, I. B. Alterman, R. B. McMullen, L. S. Cluff, and D. B. Slemmons (Editors), Vol. **292**, 45–71.

Hardebeck, J. L. (2010). Seismotectonics and fault structure of the California central coast, *Bull. Seismol. Soc. Am.* **100,** 1,031–1,050.

Hardebeck, J. L., and P. M. Shearer (2002). A new method for determining first-motion focal mechanisms, *Bull. Seismol. Soc. Am.* **92,** 2,264–2,276.

Harris, R. A., and S. M. Day (1993). Dynamics of fault interaction: Parallel strike-slip faults, *J. Geophys. Res.* **98,** no. B3, 4,461–4,472.

Harris, R. A., and S. M. Day (1999). Dynamic 3D simulations of earthquakes on en echelon faults, *Geophys. Res. Lett.* **26,** no. 14, 2,089–2,092.

Heidbach, O., M. Tingay, A. Barth, J. Reinecker, D. Kurfeß, and B. Müller (2008). The World Stress Map database release 2008, doi: 10.1594/GFZ.WSM.Rel2008.

Holzer, T. L., T. E. Noce, M. J. Bennett, J. C. Tinsley, and L. I. Rosenberg (2005). Liquefaction at Oceano, California, during the 2003 San Simeon earthquake, *Bull. Seismol. Soc. Am.* **95,** 2,396–2,411.

Irwin, W. P. (1990). Geology and plate-tectonic development, in *The San Andreas Fault System, California*, R. E. Wallace (Editor), *U.S. Geol. Surv. Profess. Pap. 1515*, 61–80.

Jachens, R. C., V. Langenheim, C. M. Wentworth, R. W. Simpson, and R. W. Graymer (2009). Defining fault offsets from aeromagnetic anomalies: Central California coast ranges, *Geol. Soc. Am. Abstracts with Programs* **41,** no. 7, 281.

Kame, N., J. R. Rice, and R. Dmowska (2003). Effects of prestress state and rupture velocity on dynamic fault branching, *J. Geophys. Res.* **108,** no. B5, ESE 13-1–ESE 13-21, doi: 10.1029/2002JB002189.

Klinger, Y., X. Xu, P. Tapponnier, J. Van der Woerd, C. Lasserre, and G. King (2005). High-resolution satellite imagery mapping of the surface rupture and slip distribution of the $M_w \sim 7.8$, 14 November 2001 Kokoxili earthquake, Kunlun fault, Northern Tibet, China, *Bull. Seismol. Soc. Am.* **95,** 1,970–1,987.

Lay, T., and T. Wallace (1995). *Modern Global Seismology*, International Geophysics Series, Vol. **58**. Academic Press, San Diego, California, 521 pp.

Downloaded from https://pubs.geoscienceworld.org/ssa/bssa/article-pdf/103/1/447/3589131/447.pdf
by University of Memphis, oluwaseun fadugba

Lettis, W. R., K. I. Kelson, J. R. Wesling, M. Angell, K. L. Hanson, and N. T. Hall (1994). Quaternary deformation of the San Luis range, San Luis Obispo County, California, in *Seismotectonics of the Central California Coast Ranges*, Geol. Soc. Am. Special Paper, I. B. Alterman, R. B. McMullen, L. S. Cluff, and D. B. Slemmons (Editors), Vol. **292**, 111–132.

Lowman, A. M. (2009). Creation of soil liquefaction susceptibility maps for San Luis Obispo & Marin Counties using geographic information systems, *Senior Thesis*, California Polytechnic State University—San Luis Obispo, California, 21 pp.

Manaker, D. M., A. J. Michael, and R. Bürgmann (2005). Subsurface structure and kinematics of the Calaveras-Hayward Fault stepover from three-dimensional V_P and seismicity, San Francisco Bay region, California, *Bull. Seismol. Soc. Am.* **95,** 446–470.

McKenzie, D. P. (1969). The relation between fault plane solutions for earthquakes and the directions of the principal stresses, *Bull. Seismol. Soc. Am.* **59,** 591–601.

McLaren, M. K., and W. U. Savage (2001). Seismicity of South-Central coastal California: October 1987 through January 1997, *Bull. Seismol. Soc. Am.* **91,** 1,629–1,658.

Miller, K. C., J. M. Howie, and S. D. Ruppert (1992). Shortening within underplated oceanic crust beneath the central California margin, *J. Geophys. Res.* **97,** 19,961–19,980.

Moore, D. E., D. A. Lockner, S. Ma, R. Summers, and J. D. Byerlee (1997). Strengths of serpentinite gouges at elevated temperatures, *J. Geophys. Res.* **102,** 14,787–14,801.

Nishenko, S. P., M. K. McLaren, W. D. Page, V. E. Langenheim, J. T. Watt, H. G. Greene, J. D. Rietman, W. R. Lettis, M. Angell, and R. Kvitek (2010). Shoreline fault zone, south-central coastal California, *Abstracts with Programs—Geol. Soc. Am.* **42,** no. 4, 82.

Nitchman, S. P., and D. B. Slemmons (1994). The Wilmar Avenue Fault: A late Quaternary reverse fault near Pismo Beach, California, in *Seismotectonics of the Central California Coast Ranges*, Geol. Soc. Am. Special Paper, I. B. Alterman, R. B. McMullen, L. S. Cluff, and D. B. Slemmons (Editors), Vol. **292**, 103–110.

Ouillon, G., C. Ducorbier, and D. Sornette (2008). Automatic reconstruction of fault networks from seismicity catalogs: Three-dimensional optimal anisotropic dynamic clustering, *J. Geophys. Res.* **113,** 15 pp., B01306, doi: 10.1029/2007JB005032.

Pacific Gas and Electric Company (PG&E) (1988). Final report of the diablo canyon long term seismic program, Report to the U.S. Nuclear Regulatory Commission, Docket Nos. 50-275 and 50-323.

Pacific Gas and Electric Company (PG&E) (2011). Report on the analysis of the Shoreline fault zone, central coastal California, Report to the U.S. Nuclear Regulatory Commission.

Page, M., K. Felzer, R. Weldon, and G. Biasi (2008). The magnitude-frequency distribution on the southern San Andreas fault follows the Gutenberg–Richter distribution (abstract S31C-06), *Eos Trans. AGU* **89,** no. 53, Fall Meet. Suppl., S31C-06.

Parsons, T., and E. L. Geist (2009). Is there a basis for preferring characteristic earthquakes over a Gutenberg–Richter distribution in probabilistic earthquake forecasting? *Bull. Seismol. Soc. Am.* **99,** 2,012–2,019.

Reinen, L. A., J. D. Weeks, and T. E. Tullis (1994). The frictional behavior of lizardite and antigorite serpentinites: Experiments, constitutive models, and implications for natural faults, *PAGEOPH* **143,** 317–358.

Schwartz, D. P., and K. J. Coppersmith (1984). Fault behavior and characteristic earthquakes: Examples from the Wasatch and San Andreas fault zones, *J. Geophys. Res.* **89,** 5,681–5,698.

Schwartz, D. P., P. J. Haeussler, G. G. Seitz, and T. E. Dawson (2012). Why the 2002 Denali fault rupture propagated onto the Totschunda fault: Implications for fault branching and seismic hazards, *J. Geophys. Res.*, doi: 10.1029/2011JB008918 (in press).

Sliter, R. W., P. J. Triezenberg, P. E. Hart, J. T. Watt, S. Y. Johnson, and D. S. Scheirer (2010). High-resolution seismic reflection and marine magnetic data along the Hosgri Fault Zone, central California, *U.S. Geol. Surv. Open-File Rept. 2009-1100*, version 1.1.

Waldhauser, F., and W. L. Ellsworth (2000). A double-difference earthquake location algorithm; method and application to the northern Hayward Fault, California, *Bull. Seismol. Soc. Am.* **90,** 1,353–1,368.

Watt, J. T., S. Y. Johnson, J. Hardebeck, D. S. Scheirer, M. A. Fisher, R. W. Sliter, and P. E. Hart (2009). Geophysical characterization of the Hosgri fault zone, central California, Central California, *Seismol. Res. Lett.* **80,** no. 2, 323.

Watt, J. T., S. Y. Johnson, and V. E. Langenheim (2011). Fault intersections along the Hosgri fault zone, central California (abstract GP41A-0977), 2011 AGU Fall Meeting, GP41A-0977.

Wells, D. L., and K. J. Coppersmith (1994). New Empirical Relationships among Magnitude, Rupture Length, Rupture Width, Rupture Area, and Surface Displacement, *Bull. Seismol. Soc. Am.* **84,** 974–1002.

Wesnousky, S. G. (2006). Predicting the endpoints of earthquake ruptures, *Nature* **444,** 358–360.

Wesnousky, S. G. (2008). Displacement and geometrical characteristics of earthquake surface ruptures: Issues and implications for seismic-hazard analysis and the process of earthquake rupture, *Bull. Seismol. Soc. Am.* **94,** 1,609–1,632.

Wiemer, S. (2001). A software package to analyze seismicity: ZMAP, *Seismol. Res. Lett.* **72,** 373–382.

Woessner, J., and S. Wiemer (2005). Assessing the quality of earthquake catalogues: Estimating the magnitude of completeness and its uncertainty, *Bull. Seismol. Soc. Am.* **95,** 684–698.

Working Group on California Earthquake Probabilities (WGCEP) (2008). The uniform California earthquake rupture forecast, version 2 (UCERF 2), *U.S. Geol. Surv. Open-File Rept. 2007-1437*.

Zhang, H., and C. H. Thurber (2003). Double-difference tomography: the method and its application to the Hayward fault, California, *Bull. Seismol. Soc. Am.* **93,** 1,875–1,889.

U.S. Geological Survey
345 Middlefield Rd.
Menlo Park, California 94025
jhardebeck@usgs.gov

Manuscript received 18 May 2012

Downloaded from https://pubs.geoscienceworld.org/ssa/bssa/article-pdf/103/1/447/3589131/447.pdf
by University of Memphis, oluwaseun, fadugba